

## Melt pool temperature and cooling rates in laser powder bed fusion

Paul A. Hooper

*Department of Mechanical Engineering, Imperial College London, SW7 2AZ, UK*



### ARTICLE INFO

**Keywords:**

High-speed thermography  
Powder bed fusion (PBF)  
Selective laser melting (SLM)  
In situ monitoring  
Temperature gradients  
Cooling rates

### ABSTRACT

In laser powder bed fusion, melt pool dynamics and stability are driven by the temperature field in the melt pool. If the temperature field is unfavourable defects are likely to form. The localised and rapid heating and cooling in the process presents a challenge for the experimental methods used to measure temperature. As a result, understanding of these process fundamentals is limited. In this paper a method is developed that uses coaxial imaging with high-speed cameras to give both the spatial and temporal resolution necessary to resolve the surface temperature of the melt pool. A two wavelength imaging setup is used to account for changes in emissivity. Temperature fields are captured at 100 kHz with a resolution of 20 μm during the processing of a simple Ti6Al4V component. Thermal gradients in the range 5–20 K/μm and cooling rates in range 1–40 K/μs are measured. The results presented give new insight into the effect of parameters, geometry and scan path on the melt pool temperature and cooling rates. The method developed here provides a new tool to assist in optimising scan strategies and parameters, identifying the causes of defect prone locations and controlling cooling rates for local microstructure development.

### 1. Introduction

Laser based metal powder bed fusion (LPBF) is an additive manufacturing (AM) process where metal powder is melted by scanning a high power laser across a powder bed. Although many would consider it a relatively mature AM technology there is still a lack of fundamental process understanding. This means that process parameter development and component design are largely conducted iteratively and empirically. Whilst this approach works, it is often slow and expensive. A deeper understanding of process fundamentals gives more information to accelerate development rather than having to rely on a best guess approach.

In situ measurements of temporally and spatially resolved melt pool temperature fields during the powder bed fusion build process have not been previously reported. The small size of the melt pool, rapid movements across the large powder bed and short duration temperature transients make it a challenging measurement problem. Determination of the melt pool temperature field can help identify regions where porosity formation is likely and assist with scan path optimisation. Cooling rates and temperature gradients during solidification can also be measured and correlated to local microstructure development. Measurements could also form part of an online quality control system with thermal histories known for every location in a component. In this paper the development of a high-speed temperature imaging system is described and the first in situ measurements of spatially and temporally resolved melt pool temperature fields are

reported.

The most detailed understanding of temperature profiles so far has come from computational modelling efforts. Khairallah et al. [1] developed a multi-physics model of LPBF which incorporated ray tracing, surface tension, Marangoni convection and recoil pressure from evaporation. The model highlighted a depression that forms under the laser due to the recoil pressure, the importance of mass transport within the melt pool and how porosity can form when the laser is turned off. Although experimental measurements of melt pool depth were used to calibrate the absorptivity of the model and high-speed imaging of the laser interaction zone have been performed [2], no experimental validation of the predicted temperature fields has been reported.

In situ process monitoring efforts have been the subject several recent reviews [3–5] and measurement of temperature has featured prominently. Coaxial measurements of radiative emissions from the melt pool have been measured using photodiodes and machine vision cameras [6,7]. Whilst these measurements provide useful process signatures for quality and process control purposes they are not calibrated for temperature and provide little insight into the underlying physical processes. An off-axis infrared camera has been used by Criales et al. [8] to measure temperature during a single scan track of a nickel alloy, however an assumed single emissivity value was relied upon meaning there could be large errors in the calculated temperature values. A wide field-of-view infrared camera has also been used to monitor the temperature of whole layers during electron beam melting (EBM) [9]. Careful calibration of local emissivity values is required and the

E-mail address: [paul.hooper@imperial.ac.uk](mailto:paul.hooper@imperial.ac.uk).

resolution and speed of this system is not sufficient to capture melt pool temperature transients.

Calibrated measurement of temperature at a single location in the melt pool has been achieved with the application of two wavelength pyrometry to LPBF [10,11]. These experiments used two photodiode detectors to measure emissions at two wavelengths and so removed the need for a priori knowledge of the emissivity of the melt pool. Whilst these detectors can provide good temporal resolution of the melt pool temperature they are limited to a single location and therefore can not determine spatial profiles. If the optics collecting light from the melt pool are not carefully aligned then off-centre temperature values will be measured. If the magnification is not sufficient then the system may collect light from an area over which the temperature is not uniform, introducing errors into the calculated temperature values.

Devesse et al. [12] developed a temperature measurement system using a hyperspectral line camera. The camera measured the intensity of light emitted from a melt pool in many spectral bands in the visible and near infrared (VNIR) region along a line profile. This allows the calculation of temperature based on the spectral profile and correction for the effects of spectral emissivity. However, as the camera measures only a line profile rather than a full area, the camera or substrate needed to be moved in order to obtain a full field temperature measurement. A steady state melt pool is also required during the scanning of an area, so its applicability to the dynamic melt pool in LPBF is limited.

Recently high-speed synchrotron X-ray imaging of the powder bed fusion process has been conducted [13]. This work shows the cross section of a stationary melt pool as it forms through to solidification. Whilst no temperature measurements have been made in this work, porosity entrapment was seen and estimates of the solidification front velocity were made from the detection of grain formation (in the order of 0.5 m/s).

In this paper the development of a new coaxial imaging setup with two high-speed cameras to give both good spatial and temporal resolution of the melt pool is described. The two wavelength imaging setup developed resolves temperature and accounts for unknown emissivity values during the material transition from powder to liquid to a bulk solid. The first measurements of fully resolved surface temperature fields are presented for a simple component with an overhanging feature; surface cooling rates and temperature gradients are also presented. The measurements made possible using this technique are expected to enable validation of powder scale modelling efforts, inform microstructure prediction codes and assist in the development of new scan strategies and parameter sets for reduced probability of defect formation. The technique can also be integrated into online process control systems, although cost of such a system is currently likely to limit industrial adoption.

The structure of the paper is as follows. First the methods section outlines the basic theory, implementation of the system on a commercial LPBF machine, image alignment and calibration of temperature measurements. A validation of the measured temperature against a type C thermocouple is also presented. Next a test geometry is described and results from locations of interest within a single build layer are presented and discussed. Limitations and sources of error are also discussed before conclusions are then drawn about the new insights gained.

## 2. Methods

### 2.1. Temperature measurement from thermal radiation

All objects above absolute zero emit thermal radiation. For an ideal black body at temperature  $T$  the spectral radiance emitted  $B$  is a function of wavelength  $\lambda$  and is described by Planck's law:

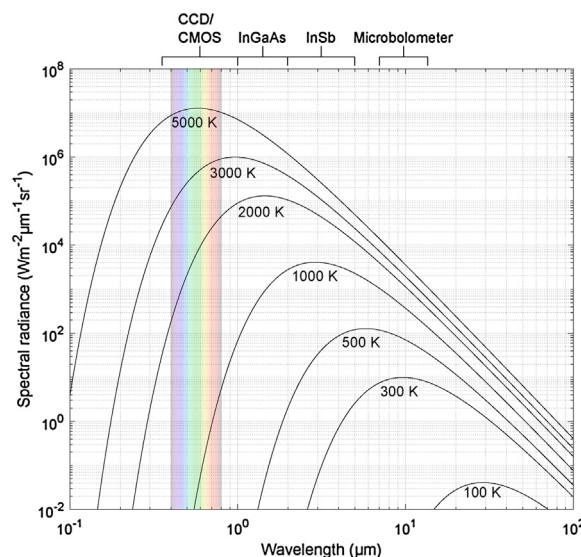


**Fig. 1.** Spectral radiance of an ideal black body at different temperatures. Wavelength sensitivity range for various sensor technologies is also shown.

$$B = \frac{2hc^2}{\lambda^5} \left( \exp\left(\frac{hc}{k_B\lambda T}\right) - 1 \right)^{-1} \quad (1)$$

where  $h$  is Planck's constant,  $c$  is the speed of light and  $k_B$  is Boltzmann's constant. Fig. 1 shows the spectral radiance of an ideal black body at different temperatures. As temperature increases the total amount of energy emitted increases and the wavelength of greatest emittance drops. The melting points of many engineering metals are above 1000 K with vaporisation temperatures in excess of 3000 K. Spectral radiance in this temperature range is strong in the VNIR part of the spectrum and therefore can be detected using conventional silicon based CCD or CMOS technology.

Real objects are rarely perfect black body emitters. Emissivity  $\epsilon$  is a parameter used to describe how well a body emits thermal radiation in comparison to an ideal black body and must have a value between 0 and 1 (1 being an ideal black body). Emissivity is dependent on material and can vary with temperature, wavelength and surface finish of an object, among other things. As a result, the emissivity value is often uncertain and this makes the direct application of Planck's law for temperature measurement difficult. To overcome this problem measurements at more than one wavelength can be made.

If two measurements of intensity  $I_1$  and  $I_2$  are made at wavelengths  $\lambda_1$  and  $\lambda_2$  then the temperature can be solved for by taking the ratio of intensities:

$$\frac{I_1}{I_2} = \frac{A_1 \epsilon_1 \lambda_2^5}{A_2 \epsilon_2 \lambda_1^5} \exp\left(\frac{hc}{k_B T} \left( \frac{1}{\lambda_2} - \frac{1}{\lambda_1} \right)\right) \quad (2)$$

where  $A_1$  and  $A_2$  are the combined efficiency of the optical path and signal detector at the two wavelengths. Eq. (2) also makes use of the Wien approximation ( $hc/\lambda \gg k_B T$ ) to simplify Planck's law for short wavelengths. By choosing wavelengths that are close, it can be assumed that the emissivities are the same  $\epsilon_1 \approx \epsilon_2$ . Once the constants  $A_1$  and  $A_2$  are known, a calibration curve can be determined which relates the intensity ratio  $I_1/I_2$  to the temperature of an object, regardless of its emissivity.

### 2.2. High-speed melt pool temperature imaging system

A commercial Renishaw AM250 metal powder bed fusion machine was modified to allow imaging of the melt pool and associated emissions along a path coaxial to the laser beam path. The coaxial imaging setup was chosen as it keeps the melt pool in the centre of the image as

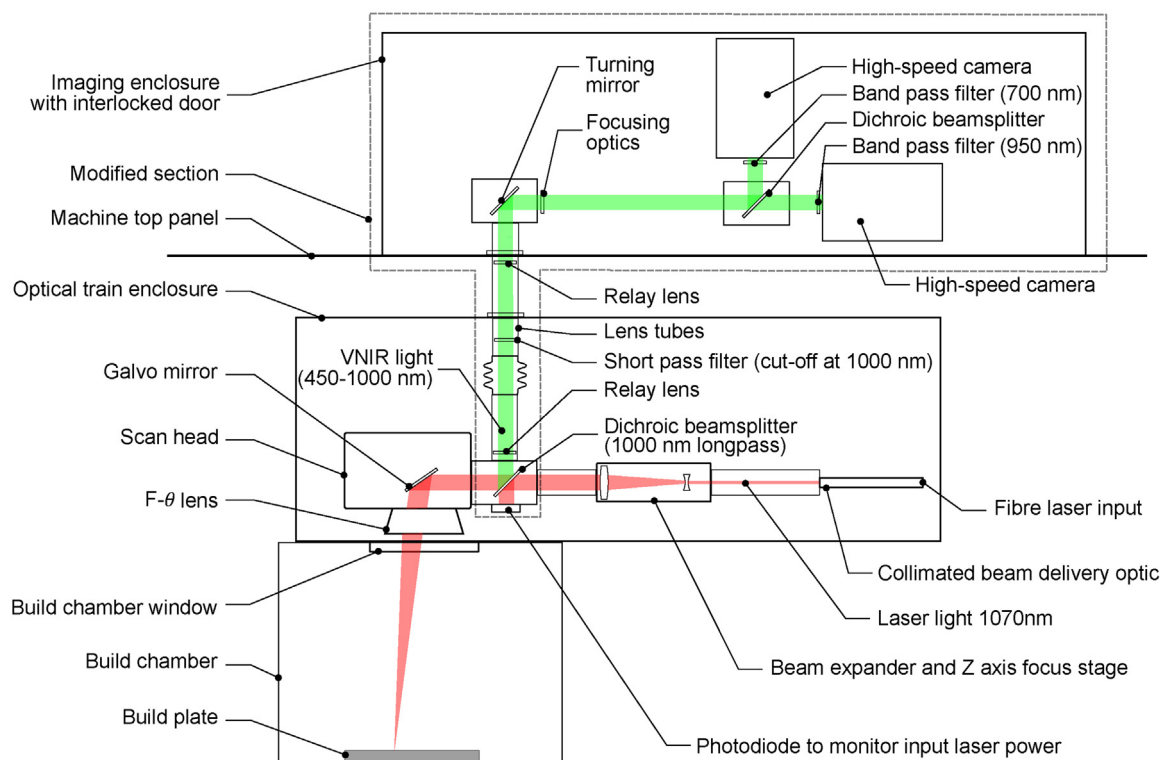


**Fig. 2.** Diagram showing optical layout of the commercial LPBF machine and modification to allow coaxial imaging of the melt pool.

the laser is scanned across the powder bed (i.e. a Lagrangian reference frame). This allows a good spatial resolution of the melt pool to be maintained across the whole build area. The decision to modify a commercial machine, rather than build a custom machine, was taken as it keeps processing conditions such as gas flow, recoating, etc. identical to that of a production environment.

Fig. 2 shows the optical layout of the machine and the modified beam path to allow coaxial imaging. A dichroic beamsplitter (Scanlab AG) was placed in the laser beam path before the scan head. This allows the light at the laser wavelength to pass through it whilst light at shorter wavelengths (such as that emitted from the melt pool zone) is reflected up into an imaging enclosure. Light is passed to the imaging enclosure via relay lenses and a short-pass filter was also used to prevent damage to imaging equipment from specular reflection of the laser. A photodiode (Thorlabs PDA10C) was placed on the reflected input side of the dichroic beamsplitter to monitor input laser power.

Inside the imaging enclosure a lens focuses the image before a second long-pass dichroic beamsplitter directs the wavelengths of interest towards the image sensors. Bandpass filters were placed in front of the image sensors to further narrow the wavelength range of interest for the two wavelength thermography analysis. Photron FASTCAM SA5 high-speed cameras were used allowing recording speed of up to 200,000 frames per second at a resolution of  $128 \times 128$  pixels with a 12 bit pixel depth. Each camera can be moved independently to account for the different focal lengths at the two wavelengths of interest. Fig. 3 shows the arrangement of optics and high-speed cameras inside the imaging enclosure.

### 2.3. Wavelengths

The choice of which wavelengths to image at is critical. Too close together and the ratio measurement will be dominated by noise from the imaging sensors; too far apart and the assumption of equal emissivity will be broken. Additional restrictions on choice of wavelength are imposed from the efficiency of coatings on optical components.

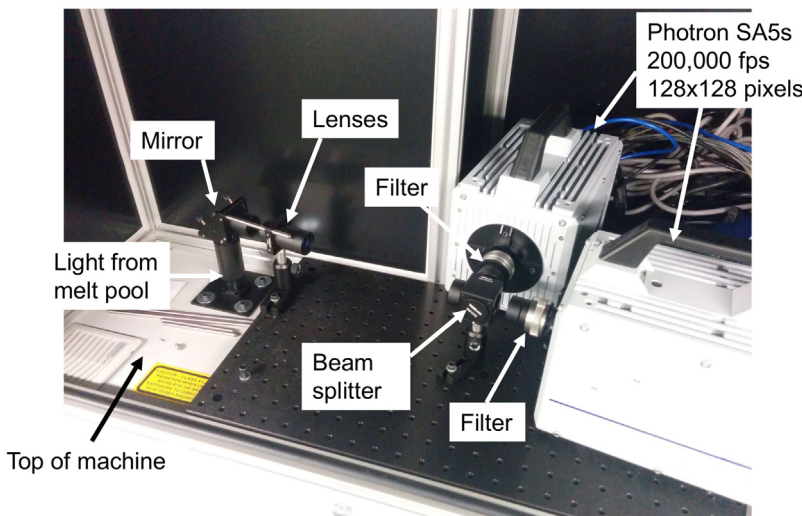
These are designed for maximum efficiency at the laser wavelength, often to the detriment of efficiency at other wavelengths. The spectral responsivity of the camera sensor also needs to be considered to ensure the maximum signal intensity is being developed and short exposure times can be used.

Fig. 4 shows the transmission efficiency spectrum from a source placed on the build platform and measured at the entrance of the imaging enclosure. It shows a very low transmission in the 750–900 nm range. This was found to be due to the optical coating used on the galvanometer scanning mirrors. Peaks in transmission efficiency were found at approximately 700 nm and 950 nm and bandpass filters were selected at these wavelengths for the two wavelength imaging system. Although the camera responsivity drops off towards 1000 nm, the black body emittance is stronger and compensates in this region except at the highest temperatures.

### 2.4. Image alignment

The optical path in the Renishaw AM250 incorporates an F-theta objective lens (LINOS Photonics GmbH) to focus the laser on a flat field at the build plate and to ensure translations in  $x$  and  $y$  position are linearly related to the angular movements of the galvanometer scanning mirrors. The combination of F-theta lens and scanning mirrors creates various optical distortions that need to be corrected for. The primary problem of concern here is that when imaging at wavelengths other than the design wavelength of the system (the laser wavelength) the optical axis is offset by a small amount that is related to the position of the scanning mirrors. The effect is that the centre of the melt pool does not appear in the centre of the image plane and moves around as the scanning mirrors change position. The offset in position is greater the further the imaging wavelength is from the design wavelength of the system. This makes it difficult to align images from both cameras before processing them in order to calculate intensity ratios for each pixel.

To align the images the position of the scanning mirrors must be known. The scan head was modified to allow recording of the position



**Fig. 3.** Photo showing high-speed cameras and optical path for two wavelength imaging.

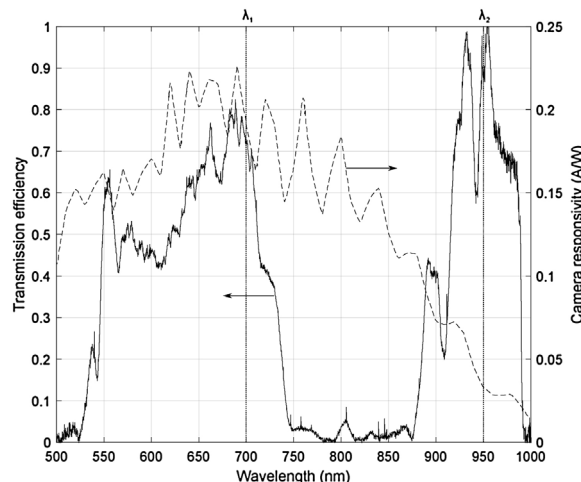


**Fig. 4.** Normalised transmission efficiency of the modified Renishaw optical path measured at the entrance to the imaging enclosure. The chosen wavelengths are indicated by  $\lambda_1$  and  $\lambda_2$ . The dashed line shows the spectral responsivity of the SA5 camera.

feedback signal used on the internal servo control boards for each mirror. A scan was then run across the entire build area and the centre of the laser in each image from each camera was identified using a 2D peak finding algorithm. It was found that the offset in position of the laser spot was linearly related and could be corrected by fitting the data to the following equations:

$$X_e = a_x + b_x x + c_x y \quad (3)$$

$$Y_e = a_y + b_y x + c_y y \quad (4)$$

where  $X_e$  and  $Y_e$  are the offsets in position at the image plane,  $x$  and  $y$  are the scan positions (location on the build plate) and  $a$ ,  $b$ , and  $c$  are wavelength dependent constants found by fitting. Calibration of the these equations allows the images to be offset in software so that they can precisely aligned before calculating the intensity ratios.

## 2.5. Calibration

To calculate temperature from the measured intensity ratio the combined efficiency of the optical path, filters and signal detector must be known at the two wavelengths (values of  $A_1$  and  $A_2$  in Eq. (2)). To achieve this a stabilised tungsten-halogen light source (Thorlabs

SLS201L) with a known spectral radiance was used to illuminate an integrating sphere. This was placed inside the build chamber and used to provide a uniform illumination source for the high-speed cameras to image. A calibrated spectrometer (Thorlabs CCS200) was used to measure the spectral radiance at the integrating sphere. The radiance measured with the spectrometer was then compared to the intensity of the image at each high-speed camera and values for  $A_1$  and  $A_2$  were calculated. An aperture stop between the light source and integrating sphere was used to reduce the intensity of the light and check for linearity of the high-speed camera sensors. The resulting calibration curve between image intensity ratio and temperature, calculated using Eq. (2), is shown in Fig. 5.

## 2.6. Validation

The temperature measured using the high-speed temperature imaging system was validated against measurements taken with a tungsten-rhenium thermocouple (type C). The thermocouple was placed inside the build chamber and aligned so that it could be heated with the laser. The chamber was then filled with argon to remove oxygen from the atmosphere and avoid embrittlement of the thermocouple. The thermocouple wires were heated approximately 0.5 mm from the junction

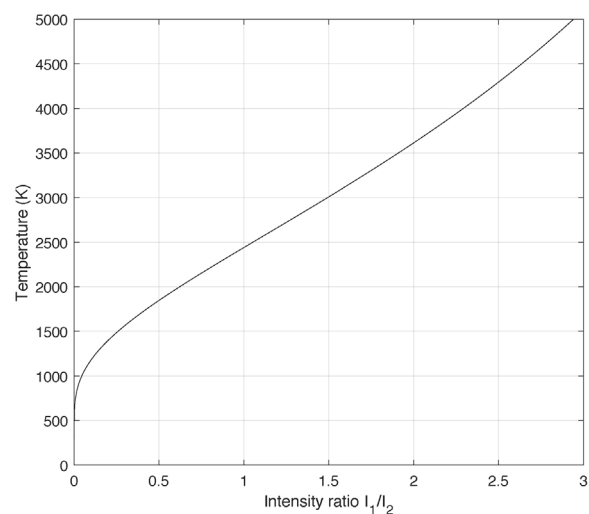


**Fig. 5.** Calibration curve showing relationship between intensity ratio and temperature.

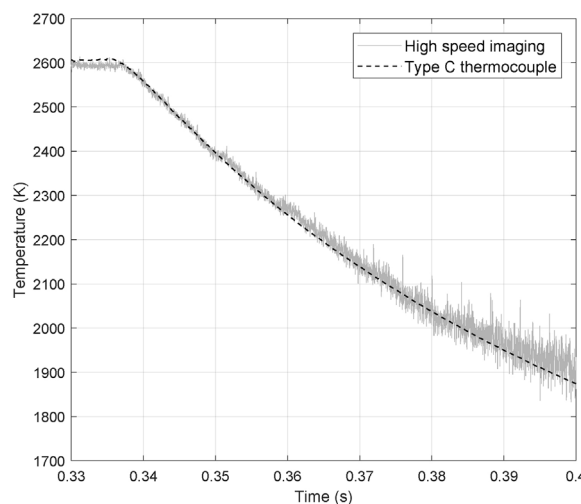


**Fig. 6.** Cooling curves showing the temperature of a type C thermocouple junction and the temperature measured using the high-speed temperature imaging system.

with a short duration (330 ms) stationary laser pulse. Heating away from the junction avoids errors due to the surface temperature being hotter than the junction temperature when the laser is on. Fig. 6 shows measured temperatures by both methods after the laser is switched off. In this temperature range a type C thermocouple is accurate to within 1%. The temperature measured using the temperature imaging system is within 1% of the thermocouple measurement with the laser on. After the laser turns off the junction cools and the noise in the temperature imaging system increases due to a reducing signal-to-noise ratio. At approximately 1900 K the measured value is still within 5% of the value determined from the thermocouple. This validation experiment shows that the technique can accurately determine temperature and that precision increases at higher temperatures.

## 2.7. Test geometry

A simple test geometry, shown in Fig. 7, was used to test the capabilities of the high-speed temperature imaging system. The part was manufactured from Ti6Al4V and has an overhanging feature and a

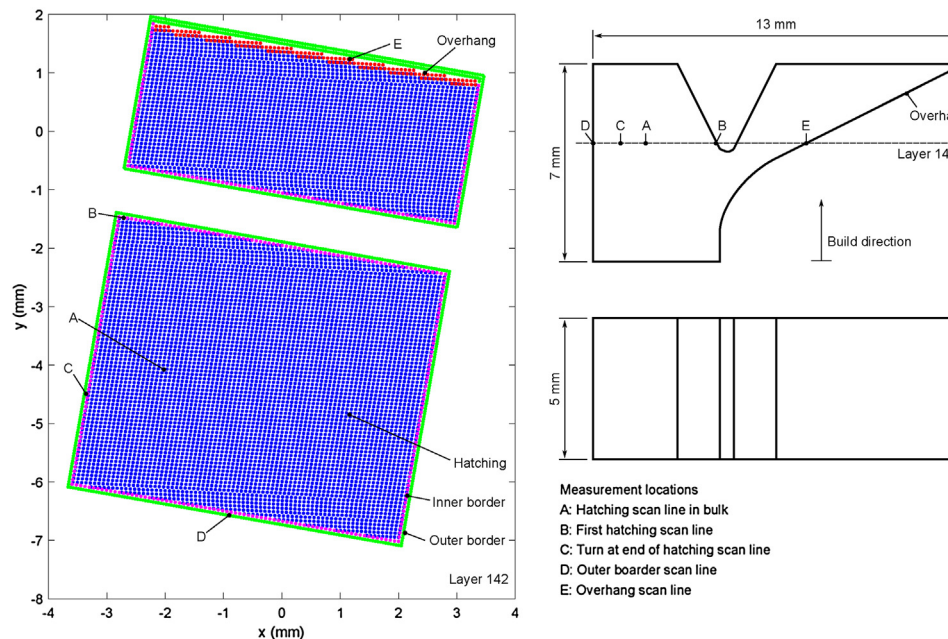


**Table 1**  
Table of requested parameters used for test geometry build in Ti6Al4V.

Parameter type	Power (W)	Point distance ( $\mu\text{m}$ )	Exposure time ( $\mu\text{s}$ )	Hatch spacing ( $\mu\text{m}$ )
Hatching	170	75	60	65
Inner border	170	75	60	—
Outer border	85	45	40	—
Overhang	155	75	60	65

notch in the top surface. These features were designed to increase the temperature in the part and demonstrate a difference in cooling rate at different locations within the part. Standard parameters provided by the machine manufacturer were used to process the part. These are listed in Table 1 and a layer height of 30  $\mu\text{m}$  was used. The Renishaw AM250 machine uses a continuous wave fibre laser (1070 nm focused to a 65  $\mu\text{m}$  spot diameter) that is power modulated to achieve a pulsed output. The scanning path is processes on a point-by-point basis and is defined by a pulse length (exposure time) and point distance (distance between exposures). For a simple comparison to continuously scanning systems the effective scan velocity can be approximated by taking the point distance and dividing by the exposure time, although this approximation ignores scanner jump and laser delays. Parameters have been optimised by the machine manufacturer for this material. The bulk of a component is scanned with the hatching parameter to provide maximum density. The hatching pattern used in this case was a bidirectional scanning pattern. The inner and outer borders are optimised for low porosity and good surface finish at the surface. The overhang parameter is of lower power to compensate for lower conductive cooling due to building on top of powder rather than bulk solid material in the overhanging region.

## 3. Results and discussion

### 3.1. Hatching parameter

The hatching parameter is used to scan the main internal area of a build layer. Fig. 8 shows the development of the surface temperature field during a single laser pulse during a hatching scan line (point A in Fig. 7) with a frame interval of 10  $\mu\text{s}$  (also shown in supplementary video bulk\_scanning.avi). The first two frames (0–10  $\mu\text{s}$ ) show the

**Fig. 7.** Test geometry and scan path for layer 142 within the sample. Each dot shows the intended position of a laser pulse and colour represents the parameter used: hatching (blue), inner border (magenta), outer border (green) and overhang (red). Scan direction for hatching is approximately parallel to the x direction. Points A-E refer to locations where results were taken from. (For interpretation of the references to color in text/this figure legend, the reader is referred to the web version of the article.)

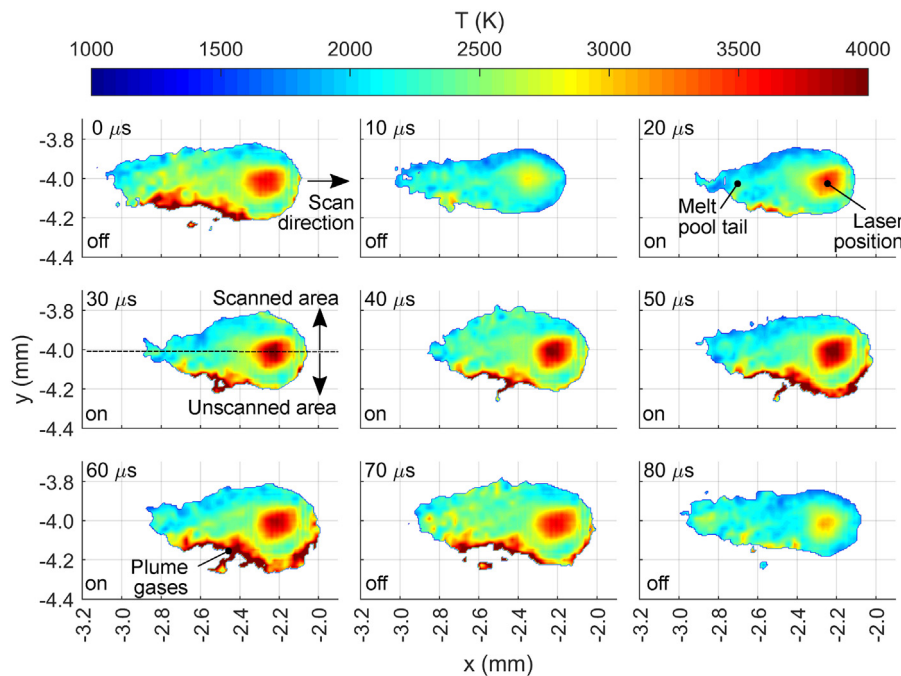


**Fig. 8.** Surface temperature sequence during a single laser pulse along a hatch scan in the bulk of the part. The laser pulse began at 13 µs and finished at 68 µs. Labels “on” and “off” indicate the status of the laser in the frame. Taken at point A in Fig. 7.

cooling of the melt pool from the previous laser pulse. There is a reduction in width and length of the melt pool and the temperature of the surface at the site of the previous laser pulse position drops to approximately 2700 K. The next laser pulse then begins at 13 µs and a rapid rise in temperature to approximately 4000 K is seen at the centre of the laser position. This is above the normal boiling point of titanium (3560 K) and the mechanism driving this is discussed in Section 3.4. Reduction in the length of the melt pool tail continues until the 40 µs frame where it has reduced to approximately 200 µm in length. The melt pool width and length then grows again until the laser pulse ends at 68 µs. The total laser on time is 5 µs shorter than the requested 60 µs and is thought to be due laser delay times added by the scanner control software. The melt pool is at its largest in the 70 µs frame and the cycle of cooling and heating then repeats.

The melt pool is relatively stable during the hatching scans of the bulk component, with occasional ejection of hot particles from the melt pool. The melt pool becomes less stable when processing close to the edge of the component. Fig. 9 (and supplementary video first\_scan\_track.avi) shows the melt development in the first hatch scan line on the layer from first pulse to last in that line (point B in Fig. 7). The initial frame is taken < 1 µs after the first pulse begins. The melt pool then grows in size to approximately 300 µm in diameter at 40 µs. There is no melt pool tail at this stage as this is the first laser pulse in the scan line. Hot plume gases (> 4000 K) are seen around the melt pool in frames 30 µs and 40 µs. These are thought to be the melt plume as they register as low brightness on the camera images, despite the high temperature calculated from the ratio images. This suggests the source is dispersed, has very low emissivity or does not follow the black body assumptions in the analysis. Upon switching the laser off an ejected particle can be seen to be forming on the edge of the melt pool in the 50 µs frame and this travels away from the melt pool in subsequent frames. The plume is larger on the second pulse due to the residual heat present in the part from the first laser pulse. As the laser scans towards the end of the track approximately 500 µm away more ejected particles can be seen and the melt pool tail can be seen to form.

Fig. 10 (and supplementary video turn\_at\_end\_of\_hatch\_line.avi) shows the surface temperature development when reversing the scan direction at the end of a hatching line at the edge of the part (point C in

Fig. 7). As the melt pool approaches the edge of the part the melt pool tail can be seen to the right of the laser position with particles being ejected from the melt pool. The galvanometer scanner then decelerates as it approaches the edge of the part and the position at which the laser pulses become closer together. In the frame at 480 µs the laser is at its furthest position before reversing direction. In this frame the tail of the melt pool is still visible on the right of the laser position as this material has not yet cooled to a temperature below the minimum detectable by the imaging system. The galvanometer scanner then begins to accelerate and the laser position begins to move in the opposite direction. The tail then forms to the left of the laser position and it continues hatching the remainder of the layer.

### 3.2. Outer border parameter

Once the hatching of an area is complete the perimeter is scanned first with an inner border then an outer border. The inner border is scanned with the same parameter as the hatching scan lines, while the outer border is scanned with a lower laser power, shorter exposure time and a smaller point distance as detailed in Table 1. This is to improve the surface finish of the final component. Fig. 11 (and supplementary video outer\_boarder.avi) shows the surface temperature during a single laser pulse when the outer border line is scanned (point D in Fig. 7). The overall size of the melt pool is smaller in comparison to the hatch parameter and temperatures are lower in magnitude. Particles are seen being ejected from the processing of the outer border but the frequency of this is less than compared to the hatch parameter. The melt pool plume is also less visible when processing this parameter. These both suggest that the melt pool is more stable during this time.

### 3.3. Overhang parameter

The overhang parameter is used on downward facing surfaces of a component. This is both to reduce the likelihood of a build failure occurring at this location and to improve the surface finish on the downward facing surface. The parameter for processing this region of the part has a reduced laser power to compensate of the lower heat conduction into the unconsolidated powder below the overhanging

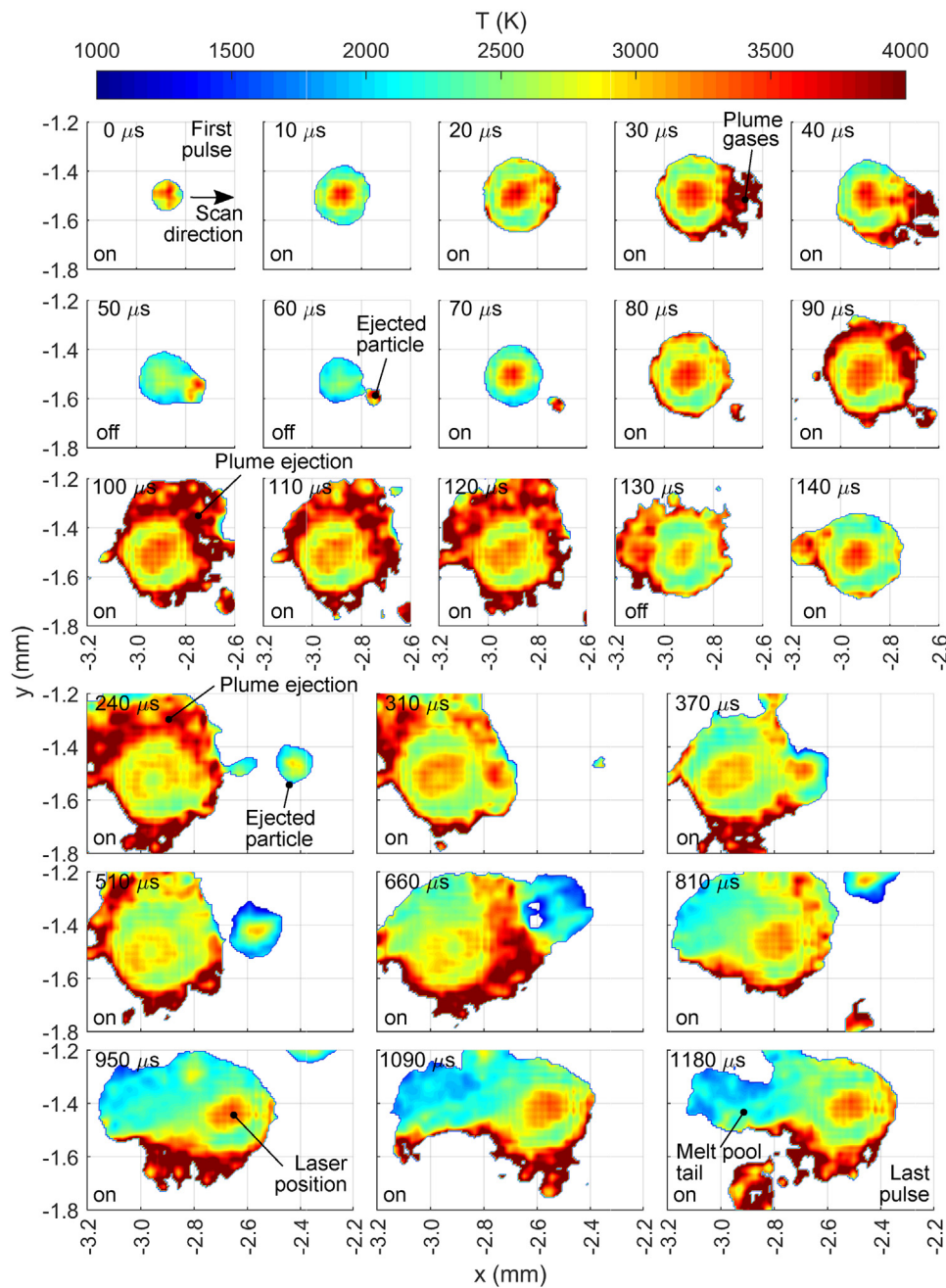


**Fig. 9.** Selected frames showing surface temperature development during scanning of the first hatching line on the layer. Labels “on” and “off” indicate the status of the laser in the frame. Taken at point B in Fig. 7.

feature. Fig. 12 (and supplementary video overhang\_scan.avi) shows the temperature field during the processing of a single overhanging scan line and the cooling after the last laser pulse in the scan line. The first three frames show the melt pool developing its tail and a large plume ejection, possibly because the galvanometer scanner is still accelerating. The melt pool then develops a long tail as it takes longer for the heat to be conducted away into the powder bed. A large number of powder particles are ejected during the last laser pulse, possibly due to the decelerating scanner or due to end of scan track effects as predicted by Khairallah et al. [1]. These ejection events cause significant heat and mass loss from the melt pool. The melt pool tail (the entire length of the scan track) can be seen to cool in the last two frames and takes in excess of 600  $\mu$ s to fully solidify.

#### 3.4. Temperature gradients and cooling profiles

The unique microstructures in PBF processes are driven by the localised high thermal gradients and rapid cooling rates during solidification. Fig. 13 shows temperature vs distance profiles from the head of the melt pool to the tail at different locations in the layer. The centre of the laser is positioned at  $x' = 0$  in each of the curves. The curves for the hatching scan in the bulk (a) and outer border scans (d) show that the peak temperature gradient is approximately 20 K/ $\mu$ m and occurs in the region outside of the laser beam diameter (65  $\mu$ m). This temperature gradient drops to approximately 5 K/ $\mu$ m as the melting temperature is approached. The overhang scan (e) shows similar characteristics but with a lower peak thermal gradient of 10 K/ $\mu$ m due to the lower thermal conductivity of the unconsolidated powder beneath the layer. The majority of the melt pool tail is at a uniform temperature,

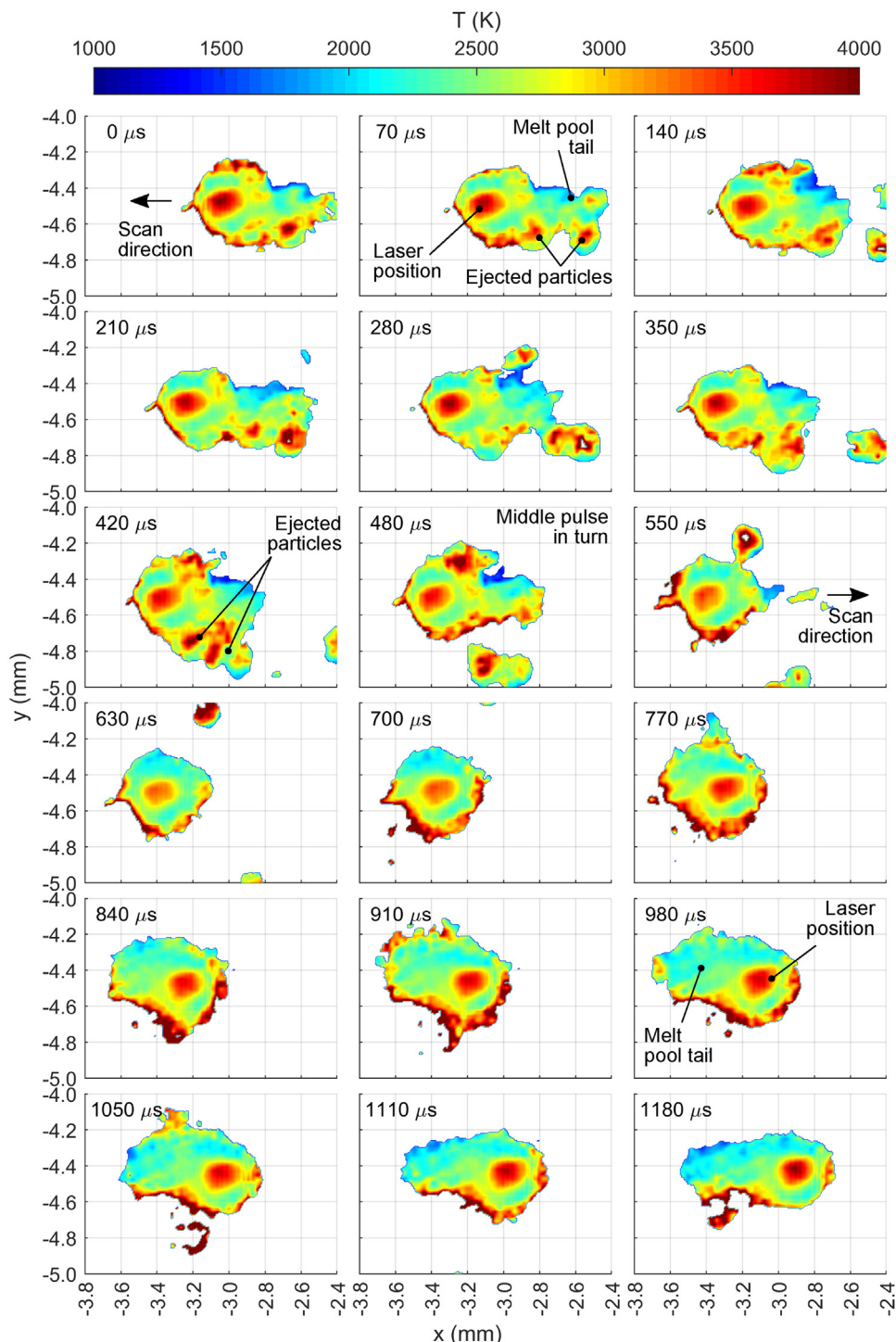


**Fig. 10.** Surface temperature sequence during a turn at the end of a hatching line. Each plot shows the temperature at a time near the end of each laser pulse as it reverses direction at the edge of the part. Taken at point C in Fig. 7.

approximately the melting temperature of Ti6Al4V. This is due to the latent heat of fusion during solidification. The temperature rapidly drops after solidification and is no longer visible with the short camera exposure time used in this experiment. The melt pool tail is at its shortest length of 400  $\mu\text{m}$  during the outer border scan, compared to 700  $\mu\text{m}$  during the hatching scan. The tail length is significantly longer during the overhanging scan at 1000  $\mu\text{m}$ . This length possibly underestimates the length during an overhang scan as this scan line was approximately 1000  $\mu\text{m}$  in total length and therefore placed a limit on the tail length.

High temperature peaks can be seen at the head of the melt pool in Fig. 13(a) and (e) and at both sides of the melt pool during the turn at the end of a scan line shown in (c). Liquid build up ahead of the laser has been predicted to occur by Khairallah et al. [1] but this is not thought to be evidence of this. It is thought to be the melt pool plume as it has a low brightness in the raw images. This is caused by the melt pool plume being forced ahead of the melt pool front by evaporation of material in the laser interaction zone. This plume may hide the observation of liquid build up ahead of the laser. It is seen from both sides of the melt pool in (d) as the laser is effectively stationary at this time.

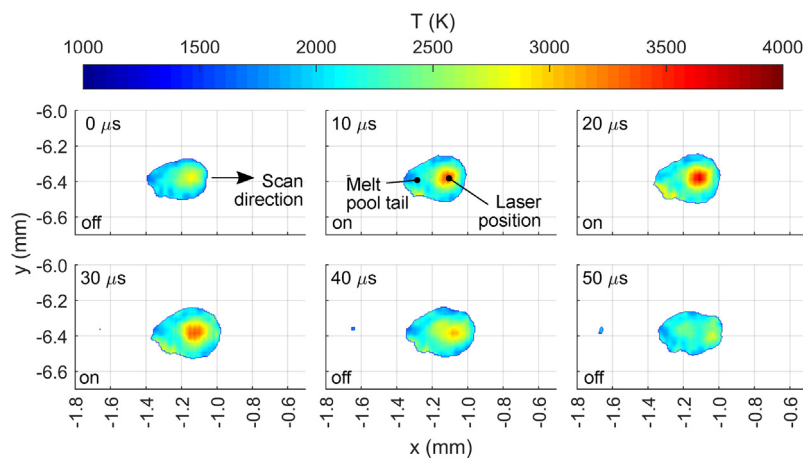


**Fig. 11.** Surface temperature sequence during a single laser pulse during an outer border scan. The laser pulse began at 2  $\mu$ s and finished at 35  $\mu$ s. Labels “on” and “off” indicate the status of the laser in the frame. Taken at point D in Fig. 7.

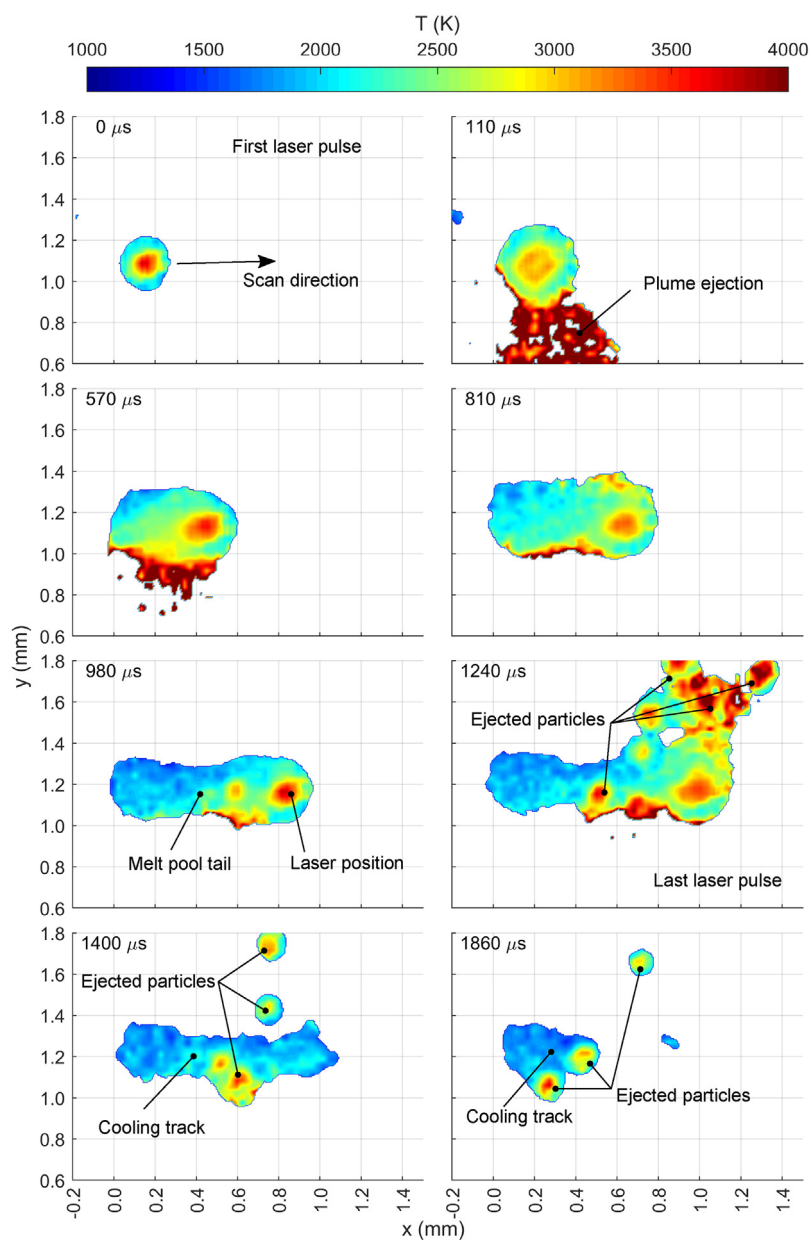


**Fig. 12.** Selected frames showing surface temperature development during scanning of an overhanging feature. Taken at point E in Fig. 7.

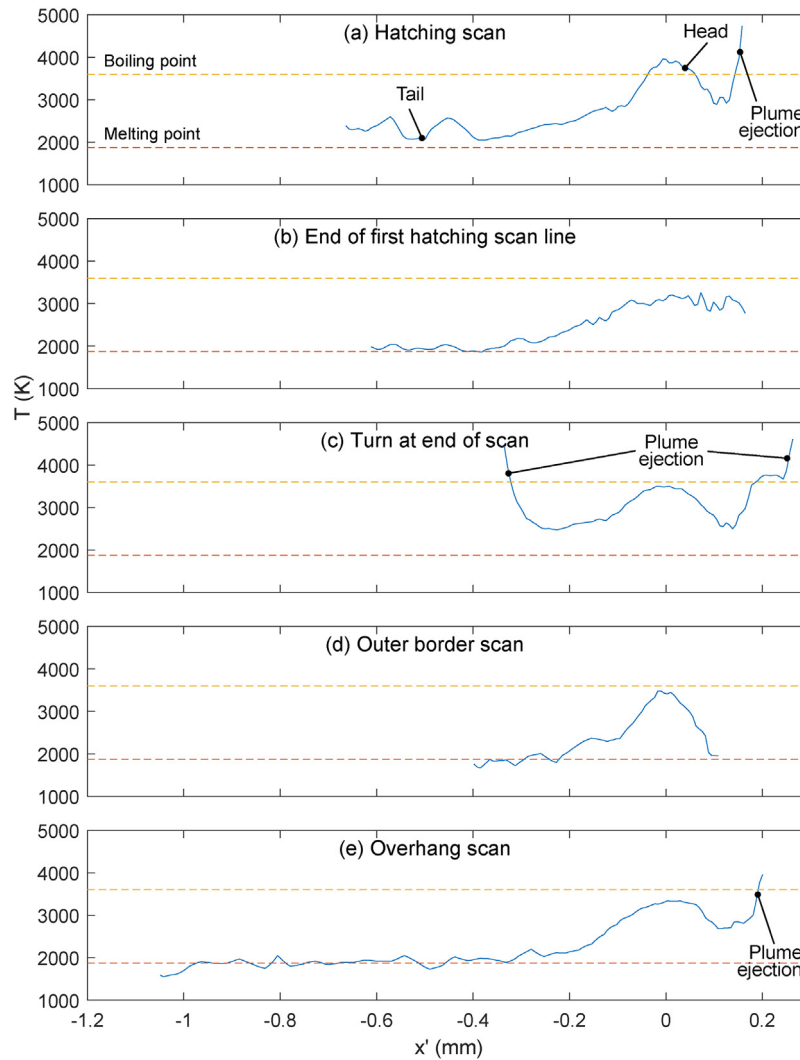


**Fig. 13.** Temperature vs distance profiles taken through a centre line drawn from the head of the melt pool to the tail for different parameter types. Profiles taken near the end of a laser pulse and  $x'$  is the distance relative to the centre of the laser beam. The horizontal dashed lines show the approximate melting and boiling point of Ti6Al4V at atmospheric pressure.

The same is not seen in (b) and (d) due to lower melt pool temperatures and reduced rate of evaporation. This caused by less build up of heat in (b) as it is the first scan line in the layer and a lower laser power in (d).

In Fig. 14 temperature-time histories of stationary locations in the build layer are plotted. In (a) the temperature-time history as a hatching scan passes over a location in the bulk of the layer is shown. Pulsing of the temperature is seen with rapid increases and decreases in temperature and is a direct result of the pulsed laser strategy used. The first two laser pulses in (a) occur as the laser approaches the measurement point, the third pulse is centred on the measurement point and for the remainder of the trace the laser is moving away from the measurement point. Before the laser passes over the measurement point the temperature raises above melting point of the material twice. As the laser moves away from the measurement point an approximate cooling rate of  $4 \text{ K}/\mu\text{s}$  is observed. The pulsing is still evident during this cooling phase, indicating that temperature waves propagate back through the melt pool. After  $500 \mu\text{s}$  the material at the measurement point solidifies and then three pulses where the temperature exceeds the melting point are observed. This either indicates re-melting of the same material or mass transport of solidified material within the melt pool due to convection currents.

When the laser is centred over the measurement point the measured melt pool surface temperature exceeds the normal boiling temperature

of the material. Semak et al. [14,15] and Ki et al. [16,17] have shown that the melt pool surface temperature need not be limited to the normal boiling point of the material due to recoil pressure at the melt surface. Ki et al. [17] predicted temperatures between 500 K and 900 K higher than the normal boiling point in laser welding of steel sheets and recoil pressures between 200 kPa and 600 kPa. Similarly Semak et al. [15] predicted peak temperatures in the region of 4000 K for iron, well above the normal boiling point of 3134 K. Khairallah et al. [1] also used similar assumptions regarding recoil pressure and reported temperatures approximately 500 K above the normal boiling point of 316L stainless steel directly under the laser spot in their numerical simulations. Although the material in this work is different, the measured increase above the normal boiling point temperature is similar to these simulations and gives confidence that the elevated temperature in the laser interaction zone is from the melt pool surface.

For the outer border scan shown in (d) similar features can be seen, with the temperature pulses reduced in length and magnitude as a result of the shorter exposure time and reduced laser power. The temperature at the measurement point spent less time at an elevated temperature and after  $300 \mu\text{s}$  dropped to the solidification temperature. This is a result of less heat being added to melt pool with every pulse whilst heat is conducted away to the surrounding material, resulting in smaller melt pool. Sub figures (b) and (e) show the cooling curves after

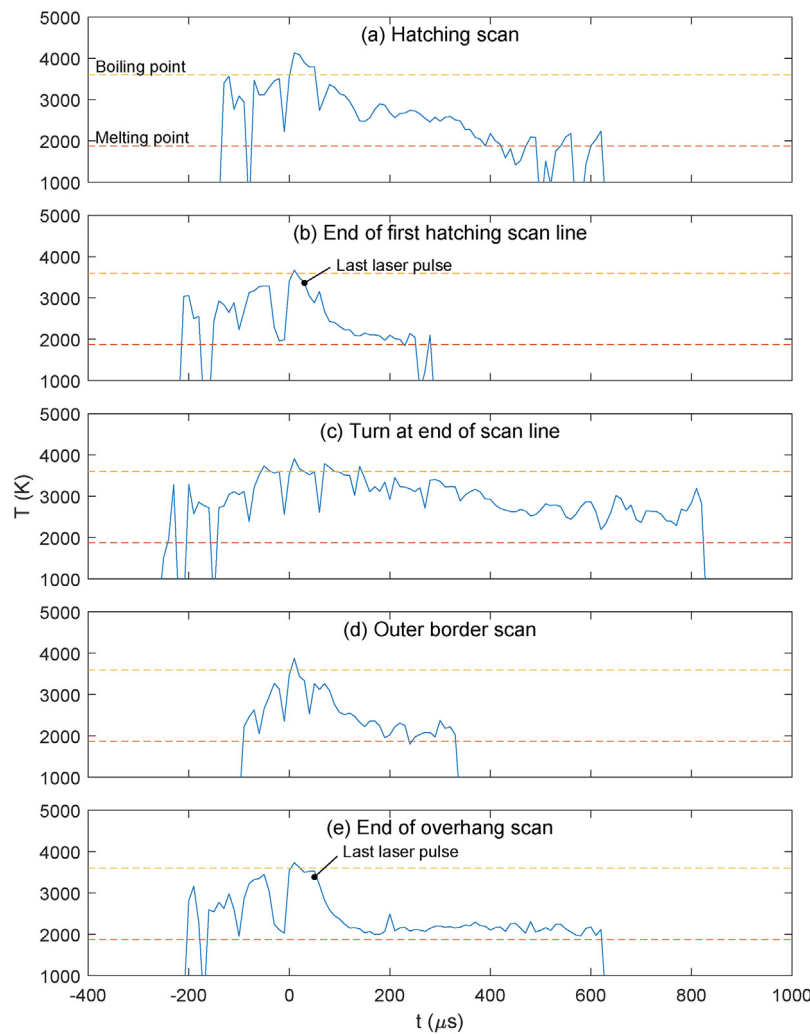


**Fig. 14.** Temperature vs time plots for fixed positions on the build plate with different parameter types. Time  $t$  has been referenced to 0 s when the laser pulses at the measurement point. Sub figures (b) and (e) show temperature at the centre of the last laser pulse at the end of a scan track. The horizontal dashed lines show the approximate melting and boiling point of Ti6Al4V at atmospheric pressure.

the last pulse in a scan line for an overhang and the first hatch line respectively. The peak cooling rate occurs immediately after the laser is switched off and is approximately  $40 \text{ K}/\mu\text{s}$ . The cooling rate slows as solidification begins and heat stored as latent heat of fusion is dissipated. Solidification takes approximately  $600 \mu\text{s}$  to finish after the last pulse in the overhang scan and  $200 \mu\text{s}$  after the last pulse in first hatch scan line, after which the temperature drops rapidly and is below the measurement range of the imaging system. For the turn at the end of the hatching scan line shown in (c) the measurement point remains at a higher temperature for a longer period of time. This is because the laser remains close to the measurement point for a longer period of time as it slows down, increments orthogonally by the hatch spacing and then starts to move away as it begins another hatch scan line. The average cooling rate during this period is  $1.5 \text{ K}/\mu\text{s}$  and the material at this point remains liquid for over  $1000 \mu\text{s}$ . The surface of the melt pool is likely to be the last part to cool as conduction is the predominant cooling method and solidification times inside the melt pool are likely to be shorter.

### 3.5. System limitations

The temperature range that can be measured by the system is determined by a number of factors. At temperatures below  $1000 \text{ K}$  relatively little light is emitted in the VNIR spectrum, the region where

conventional silicon based image sensors are sensitive. This limits the minimum detectable temperature of the system. To resolve lower temperatures a different sensor technology, such as InGaAs, would be required. However, the maximum frame rate would be limited as high-speed cameras are less developed for non-silicon based technologies.

The peak temperature of the system can be limited by saturation of either image sensor. The number of photons received by an image sensor rapidly increases with temperature as described by Planck's law. Image sensors convert the incoming photons to electrons and store them before being read out as digital values. The well depth of the sensor limits the number of electrons that can be stored. Once the storage capacity is full, further photons do not cause an increase in output signal. The user has some control over this, as the exposure time of the sensor can be set so that the signal is read out before saturation occurs. However, exposure time cannot be too short either as only a small signal will register and noise will dominate. Optical magnification is also important, increasing this by two will decrease the intensity at each pixel by four. Neutral density filters can also be used to attenuate the incoming optical intensity further if required.

The dynamic range of the camera sensor principally limits the temperature range that can be captured. This describes the ratio between the maximum and minimum detectable signals and is typically about 60 dB for a high-speed camera sensor. This corresponds to a power ratio of  $10^6$  and an approximate maximum temperature range

can found with reference to Fig. 1. It indicates that it may be necessary to choose between peak temperature and melting temperature as it may not be possible to capture both with this dynamic range. If the exposure time is increased it is possible to capture lower temperatures at the expense of some saturated pixels. One drawback is the exposure time must be set in advance, meaning that several trial runs have to be performed to set the correct exposure. In practice at a frame rate of 100 kHz and an exposure time of 10 µs (the settings used in this study) the peak pixel intensities on the camera sensor were just below their saturation point, indicating that the full dynamic range of the sensor is being used.

High-speed cameras have very high data rates and as a result store images on internal memory rather than streaming the data to a computer. This means their record time is limited and it was only possible to capture just over 3 s of image data at a time. Downloading the data takes a few minutes and therefore it is not possible to capture every layer within a build or even a whole layer if the part is large. Although the data rate is very high (20 Gbits/s per camera in this case), new interfaces and machine vision cameras are advancing rapidly and will provide options for continuous monitoring. Data processing, reduction and storage issues will also need to be addressed.

### 3.6. Sources of error

The view of the melt pool is often obscured by ejected particles and the melt pool plume. Ejected particles are easily identified in the images and the plume is only visible outside the melt pool. It is likely that the plume is also directly above the melt pool and therefore forms part of the optical path. The plume will attenuate the amount of light received by image sensors. If this attenuation is the same at both wavelengths then the ratio and temperature measurement will be unaffected. If the attenuation is stronger at one wavelength, then an error in the temperature measurement will be introduced.

The melt pool is not flat and as such the angle of incidence will vary. This is particularly true at the depression caused by vapour pressure at the laser interaction zone. Providing the emissivity at both wavelength remains equal this will not cause errors in the temperature measurement, even if the surface is not Lambertian. In the depression reflections of light emitted from within the melt pool can add to the measured intensity. If light from a surface at one temperature is reflected off a surface at another temperature then errors will be introduced to the intensity ratio and calculated temperature.

## 4. Conclusions

In this paper the first spatially and temporally resolved measurements of melt pool surface temperature in powder bed fusion were presented. The development of a two wavelength high-speed imaging thermography method was described. Temperatures in the approximate range of 1000–4000 K were captured at 100 kHz with a resolution of 20 µm. The technique was validated against measurements from a type C thermocouple. Measurements of peak temperature, melt pool size, temperature gradients and cooling rates were made. Thermal gradients in the range 5–20 K/µm and cooling rates in range 1–40 K/µs were measured and were found to vary with parameter used, component geometry and location in the scan path. Events such as beginning a scan line, ending of a scan line and turning during hatching were shown to make the melt pool more volatile and influence thermal gradients and cooling profiles. Cooling during overhang scanning took significantly longer due to the low conductivity of underlying unconsolidated powder, this was despite the reduced input laser power. This study has highlighted some of the insight gained from fully resolved melt pool surface temperature measurements. Its use allows a deeper understanding of process fundamentals and as a result can accelerate and

refine process parameter development to give improved component quality.

## Acknowledgements

The author thanks AWE plc (contract 30338995) and EPSRC (EP/K503733/1) for their financial support for this research. Thanks are also due to Adrian Eu and Seb Larsen for the their assistance in developing data processing scripts.

## Appendix A. Supplementary Data

Supplementary data associated with this article can be found, in the online version, at <https://doi.org/10.1016/j.addma.2018.05.032>.

## References

- [1] S.A. Khairallah, A.T. Anderson, A. Rubenchik, W.E. King, Laser powder-bed fusion additive manufacturing: Physics of complex melt flow and formation mechanisms of pores, spatter, and denudation zones, *Acta Mater.* 108 (2016) 36–45, <http://dx.doi.org/10.1016/j.actamat.2016.02.014>.
- [2] M.J. Matthews, G. Guss, S.A. Khairallah, A.M. Rubenchik, P.J. Depond, W.E. King, Denudation of metal powder layers in laser powder bed fusion processes, *Acta Mater.* 114 (Supplement C) (2016) 33–42, <http://dx.doi.org/10.1016/j.actamat.2016.05.017>.
- [3] S.K. Everton, M. Hirsch, P. Stravroulakis, R.K. Leach, A.T. Clare, Review of in-situ process monitoring and in-situ metrology for metal additive manufacturing, *Mater. Design* 95 (Supplement C) (2016) 431–445, <http://dx.doi.org/10.1016/j.matdes.2016.01.099>.
- [4] M. Mani, B.M. Lane, M.A. Donmez, S.C. Feng, S.P. Moylan, A review on measurement science needs for real-time control of additive manufacturing metal powder bed fusion processes, *Int. J. Prod. Res.* 55 (5) (2017) 1400–1418, <http://dx.doi.org/10.1080/00207543.2016.1223378>.
- [5] T.G. Spears, S.A. Gold, In-process sensing in selective laser melting (SLM) additive manufacturing, *Integr. Mater. Manuf. Innov.* (2016), <http://dx.doi.org/10.1186/s40192-016-0045-4>.
- [6] S. Berumen, F. Bechmann, S. Lindner, J.-P. Kruth, T. Craeghs, Quality control of laser- and powder bed-based additive manufacturing (am) technologies, *Phys. Proc.* 5 (Part B) (2010) 617–622, <http://dx.doi.org/10.1016/j.phpro.2010.08.089> Laser Assisted Net Shape Engineering 6, Proceedings of the LANE 2010, Part 2.
- [7] S. Clijsters, T. Craeghs, S. Buls, K. Kempen, J.-P. Kruth, In situ quality control of the selective laser melting process using a high-speed, real-time melt pool monitoring system, *Int. J. Adv. Manuf. Technol.* 75 (5) (2014) 1089–1101, <http://dx.doi.org/10.1007/s00170-014-6214-8>.
- [8] L.E. Criales, Y.M. Arisoy, B. Lane, S. Moylan, A. Donmez, T. Ozel, Laser powder bed fusion of nickel alloy 625: experimental investigations of effects of process parameters on melt pool size and shape with spatter analysis, *Int. J. Mach. Tools Manuf.* 121 (2017) 22–36, <http://dx.doi.org/10.1016/j.ijmachtools.2017.03.004>.
- [9] J. Mireles, C. Terrazas, S.M. Gaytan, D.A. Roberson, R.B. Wicker, Closed-loop automatic feedback control in electron beam melting, *Int. J. Adv. Manuf. Technol.* 78 (5) (2015) 1193–1199, <http://dx.doi.org/10.1007/s00170-014-6708-4>.
- [10] T. Furumoto, T. Ueda, M.R. Alkahari, A. Hosokawa, Investigation of laser consolidation process for metal powder by two-color pyrometer and high-speed video camera, *CIRP Ann.* 62 (1) (2013) 223–226, <http://dx.doi.org/10.1016/j.cirp.2013.03.032>.
- [11] M. Pavlov, M. Doubenskaia, I. Smurov, Pyrometric analysis of thermal processes in SLM technology, *Phys. Proc.* 5 (Part B) (2010) 523–531, <http://dx.doi.org/10.1016/j.phpro.2010.08.080> Laser Assisted Net Shape Engineering 6, Proceedings of the LANE 2010, Part 2.
- [12] W. Devesse, D. De Baere, P. Guillaume, High resolution temperature measurement of liquid stainless steel using hyperspectral imaging, *Sensors* 17 (2017).
- [13] C. Zhao, K. Fezzaa, R.W. Cunningham, H. Wen, F. De Carlo, L. Chen, A.D. Rollett, T. Sun, Real-time monitoring of laser powder bed fusion process using high-speed X-ray imaging and diffraction, *Sci. Rep.* 7 (1) (2017) 3602, <http://dx.doi.org/10.1038/s41598-017-03761-2>.
- [14] V. Semak, A. Matsunawa, The role of recoil pressure in energy balance during laser materials processing, *J. Phys. D: Appl. Phys.* 30 (18) (1997) 2541.
- [15] V. Semak, B. Damkroger, S. Kempka, Temporal evolution of the temperature field in the beam interaction zone during laser material processing, *J. Phys. D: Appl. Phys.* 32 (15) (1999) 1819.
- [16] H. Ki, J. Mazumder, P.S. Mohanty, Modeling of laser keyhole welding: Part I. Mathematical modeling, numerical methodology, role of recoil pressure, multiple reflections, and free surface evolution, *Metall. Mater. Trans. A* 33 (6) (2002) 1817–1830, <http://dx.doi.org/10.1007/s11661-002-0190-6>.
- [17] H. Ki, J. Mazumder, P.S. Mohanty, Modeling of laser keyhole welding: Part ii. simulation of keyhole evolution, velocity, temperature profile, and experimental verification, *Metall. Mater. Trans. A* 33 (6) (2002) 1831–1842, <http://dx.doi.org/10.1007/s11661-002-0191-5>.